

Hot Outflowing Gas from the X-ray Binary Hercules X-1

Bram Boroson

College of Wooster, Wooster, OH 44691; bboroson@acs.wooster.edu

and

Timothy Kallman

Goddard Space Flight Center, Greenbelt, MD 20771; tim@xstar.gsfc.nasa.gov

and

Saeqa Dil Vrtilek

Harvard-Smithsonian Center for Astrophysics; svrtilek@cfa.harvard.edu

Received _____; accepted _____

ABSTRACT

We present a unified picture of outflowing gas from the X-ray binary system Hercules X-1/HZ Herculis. We suggest that the outflowing gas (a wind) causes UV emission seen in mid-eclipse, narrow UV absorption lines, and broad UV P Cygni lines. Observations with the FOS and STIS spectrographs on the Hubble Space Telescope (HST) show UV emission lines in the middle of X-ray eclipse, when the X-ray heated atmosphere of the normal star and accretion disk should be entirely hidden from view. Narrow absorption lines ($\text{FWHM} \approx 50 \text{ km s}^{-1}$) blueshifted by 500 km s^{-1} during observations in 1998 and by 400 km s^{-1} during observations in 1999 were seen from $\phi = 0^\circ - 0.3^\circ$. The line velocity was constant to within 20 km s^{-1} . The P Cygni profiles from Hercules X-1 have optical depths $\tau \lesssim 1$ with a maximum expansion velocity of $\approx 600 \text{ km s}^{-1}$, and are seen in the resonance lines N V $\lambda\lambda 1238.8, 1242.8$, Si IV $\lambda\lambda 1393.7, 1402.8$, and C IV $\lambda\lambda 1548.2, 1550.8$. We discuss whether this wind originates in the accretion disk or on the companion star, and how the relevant ions can survive X-ray ionization by the neutron star.

1. Introduction

Hercules X-1/HZ Herculis is an X-ray binary consisting of a 1.24 second pulsar in an eclipsing 1.7 day orbit with a $\sim 2 M_\odot$ mass normal companion. As a result of its many periodicities, it is one of the most frequently observed X-ray binaries. The X-rays vary over a 35 day cycle; an ≈ 8 day “Main-on” state and ≈ 4 day “Short-on” state (in which the observed X-ray flux is reduced by a factor of ≈ 3) are separated by half of a 35-day phase. Outside of these states the X-ray flux is a few percent of that seen in the Main-on

state. The X-ray modulation is not due to a change in the total X-ray output, as during the X-ray low period, the optical magnitude continues to vary over the 1.7 day orbit because of X-ray heating of the companion star. Instead, the 35-day variation probably results from obscuration of the central source by an accretion disk which wobbles over a 35-day period due to an unknown cause. X-ray absorption dips occur at a period of 1.65 days, near to, but significantly greater than, the 1.62 day beat period between the 1.7 and 35 day periods (Crosa & Boynton 1981; Scott & Leahy 1999).

The far UV wavelength range is ideal for investigating the accretion disk or winds in the system, as it includes many strong resonance lines (including N V $\lambda\lambda$ 1238.8, 1242.8, Si IV $\lambda\lambda$ 1393.8, 1402.8, and C IV $\lambda\lambda$ 1548.2, 1550.8), and the continuum emission from the disk peaks in the far UV. Her X-1 was observed extensively with IUE (Dupree et al. 1978; Gursky et al. 1980; Howarth & Wilson 1983a,b; Boyle et al. 1986; Vrtilek & Cheng 1996). These investigations emphasized the orbital and 35-day variation in the line and continuum flux.

With a greater collecting area, HST could observe more subtle effects in the UV spectrum. Anderson et al. (1996) discovered that, surprisingly, even in the middle of eclipse ($\phi = 0.995 - 0.006$), emission lines of N V λ 1240, Si IV+O IV] λ 1400, N IV λ 1487, and C IV λ 1550 persist at $\approx 1\%$ of the flux seen at orbital phase $\phi = 0.5$, inferior conjunction of the neutron star. Photoionization models implied that the gas visible in mid-eclipse has a density $n_e \lesssim 10^{11} \text{ cm}^{-3}$, a temperature $15,000 \text{ K} < T < 33,000 \text{ K}$, an ionization parameter $0 \lesssim \log \xi \lesssim 1$ and an absorbing column density of $N_p \gtrsim 10^{19} \text{ cm}^{-2}$. The absence of detectable O V λ 1371 emission and the presence of N IV λ 1487 alone clearly rule out $n_e \gg 10^{11} \text{ cm}^{-3}$.

Evidence at other wavelengths supports the existence of this gas. Extended hot gas has been invoked to explain X-ray spectra during the low state (Mihara et al. 1991), and at

mid-eclipse (Parmar et al. 1985; Mavromatakis 1993; Choi et al. 1994).

UV observations of Her X-1 with the Goddard High Resolution Spectrograph (GHRS) have shown that during one HST orbit at Her X-1 orbital phase $\phi = 0.80$, the N V doublet component at 1242.8Å was stronger than the component at 1238.8Å, which should be impossible, as the oscillator strength of the 1238.8Å line is twice as strong (Boroson et al. 1996). One possible explanation for this is that there was blue-shifted P Cygni absorption associated with each doublet component, and that the 1242.8Å line could absorb the 1238.8Å line, but not vice-versa. However, this was only an indirect argument for a wind, as the blue-shifted absorption was never directly seen, and it is difficult to account for the presence of ions such as N V in a wind that may be ionized by Her X-1, with an X-ray luminosity $L_x \approx 3 \times 10^{37}$ erg s $^{-1}$.

The UV line profiles seen with the HST GHRS and Space Telescope Imaging Spectrograph (STIS) do not have the double-peaked shape expected from a Keplerian accretion disk (e.g. Smak 1969). The line profiles have been successfully fit with a model in which an accretion disk wind is responsible for the single-peak line shape (Chiang 2000, submitted).

Accretion disk winds in Cataclysmic Variables are commonly observed through P Cygni lines (Drew 1997). Such winds typically reach velocities of 3000-6000 km s $^{-1}$ with mass-loss rates of $\dot{M} \lesssim 0.05\dot{M}_{\text{acc}}$ where \dot{M}_{acc} is the white dwarf mass accretion rate. Only recently has there been any evidence for winds in low-mass X-ray binaries, however. Most of this evidence is from IR spectroscopy; for example Chakrabarty, van Kerkwijk, & Larkin (1998) have shown that there is an outflow of 250 km s $^{-1}$ with $\dot{M} \sim 10^{-6} M_{\odot}$ yr $^{-1}$ in GX 1+4/V2116 Ophiuchi. IR P Cygni lines have also been reported from Sco X-1 and GX 13+1 (Bandyopadhyay et al. 1999). Recently, *Chandra* has revealed P Cygni profiles in X-ray lines in the unusual X-ray binary Circinus X-1 (Brandt & Schulz 2000).

There have been some theoretical investigations of winds in low-mass X-ray binaries, with special attention given to Hercules X-1 (Arons 1973; Davidson & Ostriker 1973; McCray & Hatchett 1975; Basko et al. 1977; London, McCray, & Auer 1981). No consensus has been reached from the various numerical and analytic models of Hercules X-1 on whether a wind that forms from the companion’s atmosphere can provide all of the mass needed to power the X-rays from the neutron star (the “self-excited wind” model). X-ray heated and self-excited winds can have important implications for the late evolution of low-mass X-ray binaries (Ruderman et al. 1989; Iben, Tutokov, & Fedorova 1997).

Here we consider the FOS eclipse spectrum along with the results of more recent observations of the emission lines seen in eclipse and of narrow UV absorption lines (Borošon et al. 2000a, Vrtilek et al. 2001). We present the first attempt to model the P Cygni profiles of C IV, Si IV, and N V. We propose a common origin for the emission lines seen in eclipse, the narrow absorption, and the P Cygni absorption. We calculate physical parameters of the gas, speculate on its origin as a wind from the star or disk, and make predictions for further observations.

2. Observations

In 1998 and 1999, we carried out multiwavelength studies of Hercules X-1 using the HST Space Telescope Imaging Spectrograph (STIS), the Rossi X-ray Timing Explorer (RXTE), the Extreme Ultraviolet Explorer (EUVE), and ground-based observatories, including the Keck Telescope. Empirical models for the UV emission lines observed during the first segment of our campaign, in July of 1998, have been reported in Borošon et al. (2000a). The second segment of the campaign took place in July of 1999 during an “anomalous low” state in which the X-ray flux was two orders of magnitude lower than in the expected “main-on” state, although accretion continued to take place (Parmar et al.

1999).

The STIS instrument design is described by Woodgate et al. (1998), and the in-orbit performance of the STIS is described by Kimble et al. (1998). Due to the sensitivity of STIS to the radiation exposure in the South Atlantic Anomaly, STIS observations are possible only for those HST orbits that do not pass through the SAA. As a result, all of our STIS observations follow a pattern of 5 HST orbits of observations, followed by 10 HST orbits without observations.

A log of all of the HST far UV (1200–1700Å) observations of Hercules X-1 is shown in Table 1 (in the rest of the paper we will refer to observations by the labels given in Table 1). The HST observations of Her X-1 to date include 48 files for a total of 102 ksec. (Some files contain less than a complete HST orbit, as the SAA interrupted some orbits and in some cases detectors were switched in mid-orbit.) Observations extending into mid-eclipse have all been at low resolution, employing either the FOS G130H (resolution $R = \lambda/2\Delta\lambda \approx 400$) or the STIS in low-resolution mode, (G140L, $R = 960 - 1440$). The 1994 campaign described in Boroson et al. (1996) used the GHRS, alternately in low-resolution (G140L, $R \approx 1000$) and medium-resolution (G140M, $R \approx 20,000$) modes. The GHRS observations used RAPID readout mode for a time resolution of 0.1 seconds (Z2HP0202) or 0.35 seconds (all other exposures).

The remaining 29 HST orbits employed the STIS E140M grating for high resolution echelle spectroscopy. This provides a resolving power of $R = 45,800$ (6 km s^{-1}). For these exposures, we used the TIME-TAG mode on the STIS, which stamps each photon detected with a time accurate to 125 μsec . The UV continuum observed during the main-on state with the GHRS was found to pulsate with an rms amplitude of 0.4% at $\phi = 0.56$ and 0.7% at $\phi = 0.83$ (Boroson et al. 1996). During the anomalous low period, reprocessed UV pulsations were not seen, although UV quasiperiodic oscillations (QPOs) at 8 and 45 mHz

were discovered (Boroson et al. 2000b).

2.1. Mid-eclipse lines

The 1998 STIS observations included low-resolution exposures at $\phi = 0.985$ and $\phi = 0.986$ (sub-exposures of observation root name O4V401050.) Figure 1 compares these spectra with mid-eclipse spectra observed with the FOS. Both observations detect the same lines, except for the He II λ 1640 line, which is out of the wavelength coverage of the FOS. The detection of this line in mid-eclipse is not surprising, as Anderson et al. showed that the optical He II λ 4686 line also persists through mid-eclipse.

This STIS observation at mid-eclipse was at long-term phase $\Psi = 0.64$, whereas the FOS observation was at $\Psi = 0.76$. We use the definitions of the long-term phase given by Scott & Leahy (1999) from their analysis of RXTE All Sky Monitor data. The phase origin of the long-term variability, $\Psi = 0.00$, corresponds to the time of X-ray turn-on, while the length of the long-term period is assumed to be 34.853 days, or exactly 20.5 times the orbital period. The “Main High” part of the cycle then lasts from $\Psi = 0$ through $\Psi = 0.31$, following by a low state through $\Psi = 0.57$, and a “Short High” state from $\Psi = 0.57$ through $\Psi = 0.79$. The X-rays are then in the low state until the start of the next cycle (that is, they are low from $\Psi = 0.79$ through $\Psi = 1.00$.

2.2. Absorption lines

We list all detections of variable stellar absorption lines (P Cygni and narrow absorption) in Table 2. For a feature to be considered a narrow absorption line, we require that it be contained entirely within a full velocity width of 150 km s^{-1} . There is transient evidence for other narrow absorption lines, but we limit our attention to lines at

blueshifts near $400 - 500 \text{ km s}^{-1}$. The significance of a feature is higher when we have an expectation of its wavelength. When both narrow and P Cygni absorption is present, as in the 1238.8\AA line in observation O4V408040, we consider the P Cygni line to consist of the total absorption.

We integrated the absorbed flux to determine the equivalent width W_λ , velocity range, and centroid velocity. Repeating this procedure 5 times for different choices of continuum level and slope allowed us to estimate errors on these parameters.

Narrow absorption lines were detected in both N V and C IV, as shown in Figure 2 and Figure 3. We have averaged the spectra over 5 contiguous HST orbits. At $\phi = 0.14, 0.27$ the narrow absorption lines are prominent, while at $\phi = 0.59, 0.70$ their presence is obscured by broader absorption, reminiscent of P Cygni lines, which we discuss in §2.3.

It is important to note, first, that these absorption lines are stable in velocity over orbital phase. We compare the N V absorption lines at $\phi = 0.102$ (O4V406020) and at either $\phi = 0.210$ or $\phi = 0.288$ (O4V408010 or O4V408030) and find that the velocities agree to within $\pm 20 \text{ km s}^{-1}$. Between these phases, we would expect the velocity of the neutron star to differ by 60 km s^{-1} .

Second, we find that the lines are stable over periods of days. The absorption lines at O4V406020 and O4V408040, 2 days apart, agree also to within $\pm 20 \text{ km s}^{-1}$.

We have already reported the detection of absorption lines in the 1998 STIS campaign, in observations with root names O4V4030x0 (Boroson et al. 2000a). We find that the absorption line velocities are *not* stable over periods of a year. The lines appeared at a (heliocentric) velocity of -500 km s^{-1} in 1998 (O4V4030x0) and at a (heliocentric) velocity of -400 km s^{-1} in 1999 (O4V4060x0 and O4V4080x0).

The absorption line equivalent widths are variable as well. As we showed in Boroson et

al. (2000a), the differences between successive spectra do not show an increase in the amount of absorbed flux, as they would if the equivalent width were constant. For observations with root name O4V4060x0, the equivalent widths of the 1238.8Å and 1242.8Å lines were 0.30Å and 0.18Å. For O4V4080x0, these values were 0.18Å and 0.12Å. For the 1998 observations (O4V4030x0), we found equivalent widths $W_\lambda = 0.12, 0.08\text{Å}$.

It is difficult to determine whether the narrow absorption lines are present for $\phi = 0.5 - 0.6$, as they would overlap with broad P Cygni absorption (§2.3). The narrow absorption lines do *not* appear in spectra at $\phi = 0.7 - 0.8$.

2.3. P Cygni profiles

The emission lines of C IV show very clearly (Figure 4a) blue-shifted absorption that peaks at a velocity $v \approx 300 \text{ km s}^{-1}$ and extends to $v \approx 600 \text{ km s}^{-1}$. The absorption reaches a maximum optical depth $\tau = 0.8$ (here, by “optical depth” we mean simply $-\log_e(F/F_c)$.) The Si IV and N V lines also show evidence for P Cygni absorption (Figure 4b,c), although the absorption in these cases is not as clear as for C IV.

These P Cygni signatures were seen only for $\phi = 0.50 \pm 0.25$ in the 1999 data. The two HST orbits with $\phi = 0.650, 0.685$ in the 1998 data showed no P Cygni signatures.

Although the absorption feature appears directly to the blue of the narrow emission feature, and this is the classic form for a P Cygni line from an expanding envelope, the two features are not necessarily related. We show in the next section that we observe a similar broad absorption feature when the narrow emission is not seen.

2.4. P Cygni absorption without emission at $\phi = 0.10$

At $\phi = 0.10$ (O4V406020) we see an apparent gap in the broad emission lines of N V from velocities $v = -250 \text{ km s}^{-1}$ to $v = 0$ (heliocentric). This gap is filled in during the next HST orbit (at $\phi = 0.14$), as seen in Figure 5a.

The evidence suggests that this is an absorption feature, and not a deficit in emission at certain wavelengths (due for example, to a double-peaked line shape typical of emission from accretion disks). We show in Figure 5b that the O V $\lambda 1371$ line, which for reasons of atomic physics is highly unlikely to cause absorption, does not have a gap in its emission from $v = -250 \text{ km s}^{-1}$ to $v = 0$. Similarly, Figure 5e shows no such clear gap in the He II $\lambda 1640$ line, which connects excited levels. There is evidence for absorption in C IV (Figure 5d) and Si IV (Figure 5c). For these lines, the absorption is blended with the strong, constant interstellar absorption near $v = 0$.

The July 1998 STIS observations showed no such gap in emission (or absorption) near $\phi = 0.10$.

That the absorption is blueshifted at $\phi = 0.5$ suggests that the gas stream between the two stars might be responsible. Doppler tomograms, however, are not consistent with this interpretation (H. Quaintrell, personal communication). Furthermore, we have described the absorbing gas as uniformly covering the emitting region with an optical depth $\tau \approx 1$ from $\phi = 0.3$ through $\phi = 0.7$. To find the minimum portion of the emission region that needs to be covered, allowing the covering to be non-uniform, we assume that the absorption is saturated. Thus we find that at least $\approx 60\%$ of the emission region needs to be covered in order to reproduce the observation. It does not seem likely that portions of the gas stream at the same projected velocity could cover at least 60% of the heated face of HZ Her throughout the phase interval $\phi = 0.3$ to $\phi = 0.7$.

3. Identification of Line Regions: Emission, Absorption, and P Cygni Lines

First, we summarize what we know about the emission, absorption, and P Cygni features, and their orbital and random variability.

- Emission: Narrow ($\text{FWHM} \approx 150 \text{ km s}^{-1}$) emission lines probably caused by the heated atmosphere of HZ Her are seen from $\phi = 0.2$ to $\phi = 0.8$, and peak at $\phi = 0.5$. Broad ($\text{FWHM} \approx 800 \text{ km s}^{-1}$) emission lines probably caused by the accretion disk are seen at a constant flux from $\phi = 0.15$ to $\phi = 0.85$, and gradually diminish from $\phi = 0.9$ into mid-eclipse (Boroson et al. 2000a). Emission lines are seen in mid-eclipse with $\approx 1\%$ of the $\phi = 0.5$ flux, but their velocities and widths are not known.
- Absorption: Observed from $\phi = 0.1$ to $\phi = 0.3$ in both 1998 and 1999. Blue-shifted by 500 km s^{-1} in 1998 and 400 km s^{-1} (heliocentric) in 1999.
- P Cygni: Observed with maximum velocity $v_{\max} = 600 \text{ km s}^{-1}$ from $\phi = 0.25$ to $\phi = 0.70$ in 1999. Possibly observed with $v_{\max} \gtrsim 1000 \text{ km s}^{-1}$ at $\phi = 0.80$ in 1994. Possibly observed with $v_{\max} = 250 \text{ km s}^{-1}$ at $\phi = 0.10$ in 1999.

We first try to place the origin of the P Cygni lines within the system, then quantify the mass-loss rate and discuss the cause of the line variability. Finally, we relate the emission lines seen in eclipse to the narrow and P Cygni absorption lines.

We can set some limits on the origin of the P Cygni absorption. As the accretion disk contributes $\lesssim 10\%$ of the continuum near $\phi = 0.5$ during the anomalous low state in 1999, the absorption, which is deeper than 10%, must cover the normal star. At $\phi = 0.10$, the heated face of the normal star is not yet visible, and the absorption clearly covers the broad emission line which we have attributed to the accretion disk (Boroson et al. 2000a). If we were seeing the results of a disk wind covering the face of HZ Her at $\phi = 0.5$, we would

expect to see both blue and red-shifted absorption, as the wind would expand away from the neutron star. Thus it seems unlikely that we are observing the effects either of a wind close to the surface of HZ Her or a wind from the accretion disk. This leaves as a most likely explanation that the P Cygni absorption is due to a wind from the heated face of HZ Her that has expanded beyond the radius of the accretion disk.

We quantify the mass-loss rate of such a wind that is required to reproduce the observed P Cygni line optical depth. As the C IV $\lambda 1548.2$ line showed the clearest P Cygni profile, we concentrate on that line. According to the Sobolev approximation,

$$\tau = \frac{\pi e^2}{m_e c} n_p a_C g_{\text{CIV}} f \lambda (dv/dr)^{-1}, \quad (1)$$

where λ is the rest wavelength, a_C is the Carbon abundance, n_p is the proton number density, g_{CIV} is the fraction of Carbon that is ionized to C IV, e and m_e are the charge and mass of the electron, and $f = 0.19$ is the oscillator strength.

Our “observed optical depth”, $\log_e(F/F_c)$ (F is the observed flux and F_c is the continuum level) should be an approximate lower bound on the Sobolev optical depth. Except for a few complications, the Sobolev optical depth should behave like a simple optical depth in diminishing the continuum flux (see Castor 1970, Equations 7b and 20). First, in an idealized spherically expanding wind there is not only “absorption” but also “emission” (actually forward-scattered continuum photons)—this causes us to *underestimate* the true τ , as desired for a lower limit. Second, the observed absorption arises does not arise from a pointlike continuum source, and so must be averaged over impact parameter p . Equation 1 gives the *radial* optical depth, while photons from the limb of an idealized spherical continuum source encounter a transverse optical depth $\tau_0 = \tau_{\text{rad}}(1 + \sigma)$, where $\sigma = (R/v)dv/dR - 1$ (McCray et al. 1984, appendix), where Equation 1 gives τ_{rad} . If the wind velocity obeys a standard $v = v_\infty(1 - R_*/R)^\beta$ law with $\beta = 0.5 - 1.0$, then we find that the transverse optical depth should be within a factor of 3 of τ_{rad} . With these caveats,

we require that the Sobolev optical depth $\tau \gtrsim 1$, based on the observed profile.

We assume that $(dv/dr)^{-1} \sim 3 \times 10^{11} \text{ cm}/300 \text{ km s}^{-1}$ and the carbon abundance relative to hydrogen is $a_C \sim 3 \times 10^{-4}$. We also assume that the wind velocity is 300 km s^{-1} (where the absorption is the strongest). Although the wind is ionized by the X-ray source it may originate on the companion star; however we assume for simplicity that the distance from a point on the wind to the wind’s center and to the neutron star are equal, and call this r . By conservation of mass we have

$$n_p = \frac{\dot{M}}{\Omega r^2 v m_p} \approx 2 \times 10^{15} \frac{\dot{M}}{\Omega r^2} \quad (2)$$

Here, Ω is the solid angle in steradians into which the wind expands. This should be $< 4\pi$, because whether the wind originates on the star or disk, it should not be able to expand into the region in front of the star at $\phi = 0$. Together with Equation 1 this implies $\dot{M} = 2 \times 10^{-9} (r^2 \Omega / 4\pi g_{\text{CIV}}) \text{ cm}^{-2} \text{ g s}^{-1}$ and $g_{\text{CIV}} n_p = 4 \times 10^6 \text{ cm}^{-3}$. In order to know g_{CIV} , the fraction of C that is in the form C IV, we need to know the ionization parameter $\xi \equiv L_x / r_x^2 n_p$. We find $g_{\text{CIV}} = 4 \times 10^6 \xi r^2 / L_x$. We find another relation between $\log \xi$ and $\log g_{\text{CIV}}$ from simulations with XSTAR, using a power-law plus blackbody incident spectrum. Using $r = 3 \times 10^{11} \text{ cm}$ (a typical length scale for the wind, as this is the separation between the stellar atmosphere and the neutron star), the two methods give the same value of g_{CIV} at $\log \xi = 2.1$, implying $\dot{M} = 2 \times 10^{-6} \Omega / 4\pi M_\odot \text{ yr}^{-1}$. This estimated mass-loss is as great as for O supergiants, and exceeds by three orders of magnitude the accretion rate onto the neutron star. We then assume that the wind is not ionized by the full X-ray luminosity $L_x = 3 \times 10^{37} \text{ erg s}^{-1}$, but is shadowed by, for example, the disk, so that the scattered X-rays ionizing the wind have $L_x = 3 \times 10^{35} \text{ erg s}^{-1}$. We then infer $\dot{M} = 4 \times 10^{-8} \Omega / 4\pi M_\odot \text{ yr}^{-1}$. While this is still quite substantial (an order of magnitude greater than the accretion rate), it does not conflict with observations, in particular with the observed orbital period change in Her X-1 (Deeter et al. 1991). If $\Omega / 4\pi \sim 0.1$, then

$\dot{M} = 4 \times 10^{-9} M_{\odot} \text{ yr}^{-1}$, comparable to the accretion rate.

With an estimate of the wind mass-loss rate in hand, we can test the viability of the self-excited wind model. Although there is certainly an accretion disk in Hercules X-1, accretion via a wind may still play a role. For example, Friend & Castor (1982) and Blondin, Stevens, & Kallman (1991) have shown that as a mass-donor star approaches its Roche lobe, there is a continuous transition between the classical Bondi-Hoyle wind accretion and Roche lobe gas stream mass transfer.

Assuming that the wind detected in the UV lines is driven from the X-ray heated atmosphere of HZ Her, what fraction of the X-ray luminosity of Her X-1 could be powered by Bondi-Hoyle capture of the gas? The wind-accretion luminosity is given by

$$L_X = \pi \zeta r_{\text{acc}}^2 v_{\text{rel}} \rho_{\text{ns}} \frac{GM_{\text{ns}}}{R_{\text{ns}}} \quad (3)$$

Here, $\zeta \sim 0.1$ is the energy efficiency for accretion onto a neutron star, M_{ns} and R_{ns} are the mass and radius of the neutron star, ρ_{ns} is the density of the stellar wind near the neutron star, and $v_{\text{rel}} = (v_{\text{wind}}^2 + v_{\text{ns}}^2)^{1/2}$ is the velocity of the wind (with radial velocity v_{wind}) relative to the neutron star (with orbital velocity v_{ns}). The accretion capture radius r_{acc} is determined simply from the escape velocity of the neutron star by

$$r_{\text{acc}} = \frac{2GM_{\text{ns}}}{v_{\text{rel}}^2} \quad (4)$$

We use standard values of $M_{\text{ns}} = 1.4 M_{\odot}$, $R_{\text{ns}} = 10 \text{ km}$, and $v_{\text{ns}} = 169 \text{ km s}^{-1}$. We find ρ_{ns} from $\rho_{\text{ns}} = m_p n_p$ at the neutron star, assumed to be a distance $r = 3 \times 10^{11} \text{ cm}$ from the source of the wind in this case. We take $\dot{M} = 4 \times 10^{-8} \Omega / 4\pi M_{\odot} \text{ yr}^{-1}$, as found from the UV lines.

The velocity of the wind at the neutron star's orbit is not necessarily the wind's terminal velocity. There is thus a large uncertainty in the value of v_{rel} , and this has a large effect on our answer for L_X . For $v_{\text{rel}} = 300 \text{ km s}^{-1}$ we find $L_X = 2 \times 10^{37} \text{ erg s}^{-1}$, comparable

to the observed X-ray luminosity, while for $v_{\text{rel}} = 400 \text{ km s}^{-1}$, $L_X = 7 \times 10^{36} \text{ erg s}^{-1}$. Thus we conclude that *if* this wind originates in the atmosphere of HZ Her and not on the accretion disk, that it is possible for accretion of this wind to power a substantial portion or even all of the X-ray output of the neutron star.

We investigate the hypothesis that the emission at $\phi = 0$, the absorption at $\phi = 0.1 - 0.3$, and the P Cygni absorption seen at $\phi = 0.10$, $\phi = 0.3 - 0.4$, $\phi = 0.25 - 0.75$ are due to the same gas. The main argument for this hypothesis is that the narrow absorption lines (Boroson et al. 2000a and Figures 1,2) are stationary over a large fraction of the orbit. In both the 1998 and 1999 data sets, we find no detectable motion in the narrow line from $\phi = 0.1$ to $\phi = 0.3$. During this interval the velocity of the neutron star has shifted by 60 km s^{-1} . Material on HZ Her would not seem a likely candidate for the absorption line gas as at these phases, as it would not cover the broad line and continuum emission, which we attribute to the disk. Thus we expect that the absorbing gas, in common with the gas that provides the emission lines at $\phi = 0$, fills a region larger than the binary orbit.

Much of the flux in the resonance lines seen in mid-eclipse may be due to photons scattered in a wind instead of true emission. If all photons that are “absorbed” by the narrow lines are merely scattered out of our line of sight, then we expect to see a flux of scattered emission equal to the orbit-averaged absorbed flux. This would be simply the equivalent width of the line (say 0.2\AA for N $\lambda 1238.8$) times the average flux at 1237\AA (blue-shifted from the rest wavelength by $\approx 400 \text{ km s}^{-1}$). The flux available for scattering should include the continuum flux as well as the broad line emission from the accretion disk, which should extend to blue-shifts of $\approx 300 - 400 \text{ km s}^{-1}$. A reasonable estimate for this flux, from Figure 1 and Boroson et al. (2000a), is $5 \times 10^{-14} \text{ erg s}^{-1} \text{ cm}^{-2} \text{ \AA}^{-1}$. (This is valid for a first approximation only, as the equivalent widths of the absorption lines are variable, we

did not detect them from $\phi = 0.7 - 0.8$.) The total absorbed flux is then 10^{-14} erg s $^{-1}$ cm $^{-2}$. For the 1242.8Å line, which has a lower oscillator strength and absorption lines with lower equivalent width, we would expect a flux of $\approx 7 \times 10^{-15}$ erg s $^{-1}$ cm $^{-2}$. This estimate is within 50% of the observed values of the emission line flux seen in mid-eclipse (Anderson et al. 1994): $1.5, 1.2 \times 10^{-14}$ erg s $^{-1}$ cm $^{-2}$.

The problem with a scattering origin for the emission lines seen in mid-eclipse is that the N IVλ1486 and He IIλ1640 lines do not show either narrow or P Cygni absorption and from reasons of atomic physics are not expected to scatter photons. For example, the N IVλ1486 is semi-forbidden and has an oscillator strength $f = 5.74 \times 10^{-6}$ (compare with C IVλ1548.195 which has $f = 0.19$, Verner et al. 1994).

If a substantial portion of the flux in the resonance lines is the result of scattering, then the *true* emission by the wind must have a higher fraction of N IVλ1486 and He IIλ1640 relative to the resonance lines than the broad and narrow line regions. When we simulated the line emission with XSTAR using values for density and ionization stage of the emitting gas similar to those of Anderson et al., we could not obtain a UV emission spectrum enhanced in both N IVλ1486 and He IIλ1640 emission. For $\log \xi \lesssim 1.5$, N IV becomes stronger (and He II becomes weaker), while for $\log \xi \gtrsim 1.5$, He II becomes stronger (and N IV becomes weaker).

There are other scenarios that can explain the He II emission seen in mid-eclipse. For example, a strong continuum flux at He IILy β (at 256Å) could raise He to the n= 3 level and result in λ1640 emission. Using the model given by Dal Fiume et al. (1998) for the soft X-ray blackbody component to the Her X-1 spectrum, we estimate flux at 256Å of 2.5×10^{-14} erg s $^{-1}$ cm $^{-2}$ Å $^{-1}$. Given the far greater cosmic abundance of He relative to N, and that the oscillator strengths of He IILy β and N Vλ1238.8, 1242.8 are of the same order of magnitude, it does not seem unreasonable for He IILy β to have an

equivalent width of $\sim 1\text{\AA}$, which could produce the observed He II λ 1640 emission flux of $1.2, 1.1 \times 10^{-14} \text{ erg s}^{-1} \text{ cm}^{-2}$ in mid-eclipse.

Furthermore, optical He II λ 4686 emission is seen in mid-eclipse (Anderson et al. 1994; Still et al. 1997). A similar emission mechanism may be responsible for this line, and in fact, each He II electron that goes from n=4 to n=3 (emitting a 4686\AA photon) may then go down to the n=2 level and emit a 1640\AA photon. From the observed flux of He II λ 4686, $5 \times 10^{-15} \text{ erg s}^{-1} \text{ cm}^{-2}$, we would then infer a He II λ 1640 flux of $1.4 \times 10^{-14} \text{ erg s}^{-1} \text{ cm}^{-2}$.

Thus it is possible that the permitted resonance lines seen in mid-eclipse are actually scattered, in which case we would expect them to be red-shifted. Scattering can only occur from surrounding regions that have a direct view of parts of the system that are bright in the UV (the disk and heated face of the star). If the gas is blue-shifted when it is in front of the emission, causing the narrow absorption lines, it should be red-shifted at $\phi = 0$. If the He II line is formed by radiative excitation to the n=3 or higher levels, then it should be emitted only by portions of the wind in view of the soft X-ray source, and thus should also be red-shifted in mid-eclipse.

Although Anderson et al. suggested tentatively that the lines seen in mid-eclipse were redshifted, the redshift was comparable to the accuracy of the FOS wavelengths. The line profiles at $\phi = 0.057, 0.065$ observed with the STIS (O4V403010 and O4V406010) show both a blue-shifted component and a weaker red-shifted component (extending to $\approx 400 \text{ km s}^{-1}$) in N V and C IV. The blue-shifted component may arise from the receding part of the disk (the first to emerge from mid-eclipse), and the red-shifted component may be the same as that seen in mid-eclipse, as the line fluxes are similar. We have fit the lines seen in mid-eclipse with the STIS in low resolution with Gaussians. The lines are near rest velocity or slightly blueshifted ($\sim 100 \text{ km s}^{-1}$), but there are large systematic errors associated with fitting doublets with absorption lines that may overlap the emission. Further observations

of the lines seen in mid-eclipse should clarify the contribution of scattering to the emission.

The P Cygni lines are variable, appearing only at $\phi \approx 0.25 - 0.75$, and only in absorption at $\phi = 0.1$. Furthermore, these features do not always appear at these phases, and may be absent outside of the anomalous low state of 1999. Are they variable because the outflow starts and stops, or because the illumination of the wind by X-rays is variable? The previous calculation shows that a more reasonable value of \dot{M} follows if we assume that the P Cygni profile can only form where the wind is shadowed from direct X-ray illumination. Furthermore, the absorption at $\phi = 0.10$ disappears by $\phi = 0.14$. With an observed maximum line-of-sight wind velocity of 250 km s^{-1} , the leading edge of the wind would travel by just $2 \times 10^{11} \text{ cm}$, the radius of the accretion disk, between the end of one observation and the start of the next. Thus it seems more likely that the absorbing material has been ionized than that the flow has become unsteady.

The similarity in velocities between the narrow absorption lines and the broader P Cygni absorption features suggests a physical link. Perhaps the narrow absorption lines arise in gas that is coasting after having already been accelerated in the region that causes the P Cygni lines.

4. Future Work

We are experimenting with hydrodynamic models of a wind in Hercules X-1. From the output of these models, we will predict the UV emission and absorption line profiles as a function of orbital phase. We hope that this will help us distinguish the observational signatures of winds from the accretion disk and winds from HZ Her.

The narrow resonance emission lines may be emitted or scattered in a wind. Examination of the velocities of gaussian fits to the narrow lines (Boroson et al. 2000a)

shows that they do not match the expected velocity of the X-ray heated, visible face of HZ Her (Boroson et al. 1996). Doppler tomograms of the narrow lines (Vrtilek et al. 2001) place them on one side of the face of HZ Her; however with this placement the lines would be brighter at $\phi = 0.25$ than at $\phi = 0.75$. The observed lines behave in exactly the opposite manner, and are ~ 4 times brighter at $\phi = 0.75$. Non-resonance lines, less likely to be formed by scattering, show tomograms more evenly spread throughout the Roche lobe of HZ Her. One possible explanation for the difficulty in matching the narrow line velocity with a model is that the velocity of the narrow lines is not determined simply from the system's 1.7 day rotation. We will investigate the possibility that the narrow line profile is affected by the motion of a wind in a future paper.

5. Acknowledgements

Based on observations with the NASA/ESA *Hubble Space Telescope*, obtained at the Space Telescope Science Institute, which is operated by the Association of Universities for Research in Astronomy, Inc., under NASA contract GO-05874.01-94A. SDV supported in part by NASA (NAG5-2532, NAGW-2685), and NSF (DGE-9350074). BB acknowledges an NRC postdoctoral associateship.

REFERENCES

- Anderson, S.F., Wachter, S., Margon, B., Downes, R.A., Blair, W.P., & Halpern, J.P. 1994, ApJ, 436, 319
- Arons, J. 1973, ApJ, 184, 539
- Bandyopadhyay, R.M., Shahbaz, T., Charles, P.A., & Naylor, T. 1999, MNRAS, 306, 417
- Basko, M.M., Sunyaev, R.A., Hatchett, S., & McCray, R. 1977, ApJ, 215, 276
- Basko, M.M., Sunyaev, R.A., & Titarchuk, L.G. 1974, A&A, 31, 249
- Blondin, J.M., Stevens, I.R., & Kallman, T.R. 1991, ApJ, 371, 684
- Boroson, B., Kallman, T., Vrtilek, S.D., Raymond, J., Still, M., Bautista, M., & Quaintrell, H. 2000a, ApJ, 529, 414
- Boroson, B., Vrtilek, S.D., McCray, R., Kallman, T., & Nagase, F. 1996, ApJ, 473, 1079
- Boyle, S.J., Howarth, I., Wilson, R., & Raymond, J. 1986, in New Insights in Astrophysics: 8 Years of UV Astronomy with IUE, ed. E.J. Rolfe (Noordwijk: ESA), 471
- Brandt, W.N., & Schulz, N.S. 2000, ApJ, submitted
- Castor, J. 1970, MNRAS, 149, 111
- Chakrabarty, D., van Kerkwijk, M.H., & Larkin, J.E. 1998, ApJ, 497, L39
- Clark, R.E.H., Magee, N.H. Jr., Mann, J.B., & Merts, A.L. 1982, ApJ, 254, 412
- Crosa, L., & Boynton, P.E. 1980, ApJ, 235, 999
- Davidson, K., & Ostriker, J.P. 1973, ApJ, 179, 585
- Deeter, J.E., Boynton, P.E., Miyamoto, S., Kitamoto, S., Nagase, F., & Kawai, N. 1991, ApJ, 383, 324

- Drew, J. 1997, in Accretion Phenomena and Related Outflows, IAU Colloquium 163, ASP Conference Series, Vol. 121. D.T. Wickramasinghe, L. Ferrario, & G.V. Bicknell, eds.
- Dupree, A.K. et al. 1978, *Nature*, 275, 400
- Friend, D.B., & Castor, J.I. 1982, *ApJ*, 261, 293
- Gursky, H. et al. 1980, *ApJ*, 237, 163
- Howarth, I., & Wilson, R. 1983a, *MNRAS*, 202, 347
- Howarth, I., & Wilson, R. 1983b, *MNRAS*, 204, 1091
- Iben, I., Tutukov, A.V., Federova, A.V. 1997, *ApJ*, 486, 955
- London, R., McCray, R., & Auer, L.H. 1981, *ApJ*, 243, 970
- McCray, R., & Hatchett, S. 1975, *ApJ*, 199, 196
- Mihara, T., Makishima, K., Ohashi, T., Sakao, T., & Tashiro, M. 1990, *Nature*, 346, 250
- Parmar, A.N., Oosterbroek, T., Dal Fiume, D., Orlandini, M., Santangelo, A., Segreto, A., & Del Sarda, S. 1999, *A&A*, 350, L5
- Ruderman, M., Shaham, J., Tavani, M., & Eichler, D. 1989, *ApJ*, 343, 292
- Scott, D.M. & Leahy, D.A. 1999, *ApJ*, 510, 974
- Smak, J. 1969, *Acta Astron.*, 19, 155
- Verner, D.A., Barthel, P.D., Tytler, D. 1994, *A&AS*, 108, 287
- Vrtilek, S.D., & Cheng, F.H. 1996, *ApJ*, 465, 915
- Vrtilek, S.D., Quaintrell, H., Boroson, B., Still, M., Fiedler H., O'Brien, K., Raymond, J.R., Kallman, T., & McCray, R. 2001, *ApJ*, 548, 471

Woodgate, B.E. et al. 1998, PASP, 110, 1183

Fig. 1.— Top panel: FOS spectrum of Her X-1 from a 1600 s exposure spanning $\phi = 0.995 - 0.006$. The strong emission line at 1216Å is geocoronal, and not intrinsic to Her X-1. Bottom panel: a 444 s STIS exposure spanning $\phi = 0.984 - 0.990$.

Fig. 2.— Narrow absorption lines in N V $\lambda\lambda$ 1238.8, 1242.8. Vertical dotted lines mark a heliocentric velocity of -400 km s^{-1} . (a) Observations with abbreviated root name 80x0 (solid line, see Table 2 for observation root names), with average phase $\phi = 0.27$, and with root name 60x0 (dot-dashed line), with $\phi = 0.14$. (b) Observations with root name 70x0 (solid line), with $\phi = 0.70$, and with root name 50x0 (dot-dashed line), with $\phi = 0.59$.

Fig. 3.— Narrow absorption lines in C IV $\lambda\lambda$ 1548.195, 1550.77. There are strong interstellar absorption lines near the rest wavelengths of the C IV lines. Vertical lines mark a heliocentric velocity of -400 km s^{-1} . (a) Observations with root name 80x0 (solid line), with average phase $\phi = 0.27$, and with root name 60x0 (dot-dashed line), with $\phi = 0.14$. (b) Observations with root name 70x0 (solid line), with $\phi = 0.70$, and with root name 50x0 (dot-dashed line), with $\phi = 0.59$.

Fig. 4.— P Cygni line profiles in the UV spectrum of Hercules X-1. We have averaged the orbits with root name O4V50x0 and 7010, 7020, 7030. (a) C IV $\lambda\lambda$ 1548, 1550 (strong ISM absorption lines appear at the rest wavelengths of the lines), (b) Si IV $\lambda\lambda$ 1393, 1403 (and a blend of O IV and Si IV lines), and (c) N V $\lambda\lambda$ 1238.8, 1242.8.

Fig. 5.— A comparison of the line profiles at $\phi = 0.10$ (solid line) and $\phi = 0.14$ (dot-dashed line), showing absorption at velocities from $v = -250 \text{ km s}^{-1}$ to $v = 0$. (a) N V $\lambda\lambda$ 1239, 1243, (b) O V λ 1371, (c) Si IV $\lambda\lambda$ 1393, 1403, (d) CIV $\lambda\lambda$ 1548, 1551, (e) He II λ 1640. The top x-axis marks the heliocentric velocity; for the doublets we use the blue component.

Fig. 6.— We sketch the components of the Her X-1 system, including HZ Her, the neutron star (marked with X), the accretion disk, and the gas stream. The UV continuum is emitted

mostly from the heated face of HZ Her, as shown. At $\phi = 0.5$, the UV emission is absorbed by approaching gas, and is blue-shifted. P Cygni absorption is caused by gas close to the system that is still accelerating, while narrow absorption is caused by gas further out that coasts at the wind's terminal velocity.

Table 1. HST Far UV Observations of Hercules X-1

Root name	Instrument ^a	Start (MJD) ^b	Exposure (s)	Orbital Phase ^c
Y0XI0201	FOS H	48742.573	1600	0.458
Y0XI0204	FOS H	48748.595	1600	0.961
Z2HP0202	GHRS L	49591.134	1266	0.559
Z2HP0204	GHRS L	49591.199	729	0.596
Z2HP0206	GHRS M	49591.267	2311	0.641
Z2HP0208	GHRS M	49591.333	2474	0.680
Z2HP020A	GHRS L	49591.400	911	0.715
Z2HP020C	GHRS L	49591.413	963	0.723
Z2HP020E	GHRS M	49591.467	2431	0.760
Z2HP020G	GHRS M	49591.534	2475	0.799
Z2HP020I	GHRS L	49591.601	911	0.833
Z2HP020K	GHRS L	49591.614	969	0.841
Z2HP020M	GHRS M	49591.669	2413	0.878
Z2HP020O	GHRS M	49591.735	1585	0.914
O4V401010	STIS L	51004.563	565	0.904
O4V401020	STIS L	51004.572	1517	0.913
O4V401030	STIS L	51004.623	1495	0.944
O4V401040	STIS L	51004.646	1702	0.967
O4V401050	STIS L	51004.702	444	0.985
O4V403010	STIS E	51006.514	2227	0.057

Table 1—Continued

Root name	Instrument ^a	Start (MJD) ^b	Exposure (s)	Orbital Phase ^c
O4V403020	STIS E	51006.572	2636	0.092
O4V403030	STIS E	51006.639	2636	0.132
O4V403040	STIS E	51006.706	2636	0.171
O4V403050	STIS E	51006.773	2620	0.211
O4V404010	STIS E	51007.522	2227	0.650
O4V404020	STIS E	51007.580	2636	0.685
O4V404030	STIS E	51007.647	2636	0.725
O4V404040	STIS E	51007.714	2636	0.764
O4V404050	STIS E	51007.781	2620	0.804
<hr/>				
O4V405010	STIS E	51371.124	2227	0.512
O4V405020	STIS E	51371.185	2636	0.549
O4V405030	STIS E	51371.253	2636	0.589
O4V405040	STIS E	51371.321	2636	0.629
O4V405050	STIS E	51371.388	2620	0.669
O4V406010	STIS E	51372.064	2227	0.065
O4V406020	STIS E	51372.124	2636	0.102
O4V406030	STIS E	51372.193	2636	0.142
O4V406040	STIS E	51372.260	2636	0.182
O4V406050	STIS E	51372.328	2620	0.221

Table 1—Continued

Root name	Instrument ^a	Start (MJD) ^b	Exposure (s)	Orbital Phase ^c
O4V407010	STIS E	51373.004	2227	0.618
O4V407020	STIS E	51373.065	2636	0.655
O4V407030	STIS E	51373.133	2636	0.695
O4V407040	STIS E	51373.200	2636	0.735
O4V407050	STIS E	51373.268	2620	0.774
O4V408010	STIS E	51374.011	2227	0.210
O4V408020	STIS E	51374.072	2636	0.247
O4V408030	STIS E	51384.140	2636	0.288
O4V408040	STIS E	51374.207	2620	0.327

^aL means low resolution, M means medium resolution, H means high resolution, and E means echelle mode

^bIn terms of calendar day, the FOS observations took place April 30 and May 6, 1992, the GHRS observations took place August 27, 1994, the STIS observations O4V401010 through 4050 took place from July 10-15, 1998, and STIS observations O4V405010 through O4V408030 took place from July 12-15, 1999.

^cThe orbital phase of the mid-exposure time, using the ephemeris of Deeter et al. (1991)

Table 2. Hercules X-1 Absorption Lines

Root name	Phase ^a	Line ^b	W_λ	Type ^c	V range ^d
O4V403020	0.092	N VB	0.15±0.01	N	-513±1, (-572,-470)±(1, 10)
O4V403020	0.092	N VR	0.094 ± 0.006	N	-503±2, (-550,-460)±(20, 10)
O4V403030	0.132	N VB	0.085±0.006	N	-510±2, (-550,-460)±(20, 10)
O4V403030	0.132	N VR	0.060±0.009	N	-500±1, (-540,-450)±(10, 10)
O4V403040	0.171	N VB	0.091±0.03	N	-494±5, (-560,-430)±(10, 10)
O4V403040	0.171	N VR	0.064±0.005	N	-515±2, (-560,-490)±(20, 20)
O4V405010	0.512	N VB	0.60 ± 0.04	P	(-520,-200)±(5, 20)
O4V405010	0.512	Si IVB	0.53 ± 0.01	P	(-520,-100)±(10, 10)
O4V405010	0.512	C IVB	0.79 ± 0.06	P	(-600,-160)±(30, 10)
O4V405020	0.549	N VB	0.52 ± 0.01	P	(-550,-260)±(10, 10)
O4V405020	0.549	Si IVB	0.25 ± 0.02	P	(-520,-160)±(10, 10)
O4V405020	0.549	C IVB	0.58 ± 0.07	P	(-530,-210)±(30, 10)
O4V405030	0.589	N VB	0.34 ± 0.03	P	(-520,-270)±(40, 10)
O4V405030	0.589	Si IVB	0.17 ± 0.02	P	(-560,-200)±(10, 40)
O4V405030	0.589	C IVB	0.57 ± 0.05	P	(-500,-220)±(10, 10)
O4V405040	0.629	N VB	0.30 ± 0.04	P	(-530,-280)±(10, 10)
O4V405040	0.629	Si IVB	0.09±0.05	P	(-590,-190)±(60, 10)
O4V405040	0.629	C IVB	0.37 ± 0.03	P	(-480,-260)±(10, 10)
O4V405050	0.669	N VB	0.28 ± 0.02	P	(-530,-290)±(100, 10)
O4V405050	0.669	Si IVB	0.08 ± 0.01	P	(-510,-340)±(30, 10)

Table 2—Continued

Root name	Phase ^a	Line ^b	W_λ	Type ^c	V range ^d
O4V405050	0.669	C IVB	0.31 ± 0.05	P	(-450,-280) $\pm(10,10)$
O4V406020	0.102	N VB	0.71 ± 0.01	P?	(-280,30) $\pm(10,10)$
O4V406020	0.102	N VR	0.56 ± 0.04	P?	(-260,0) $\pm(10,10)$
O4V406020	0.102	N VB	0.21 ± 0.02	N	-394 ± 1 , (-440,-350) $\pm(10,10)$
O4V406020	0.102	C IVB	0.20 ± 0.01	N	-380 ± 1 , (-430,-340) $\pm(10,10)$
O4V406020	0.102	C IVR	0.17 ± 0.02	N	-394 ± 1 , (-430,-360) $\pm(10,10)$
O4V406030	0.142	N VB	0.22 ± 0.02	N	-393 ± 3 , (-440,-340) $\pm(10,10)$
O4V406030	0.142	C IVB	0.23 ± 0.01	N	-394 ± 1 , (-440,-350) $\pm(10,10)$
O4V406030	0.142	C IVR	0.17 ± 0.01	N	-400 ± 1 , (-440,-350) $\pm(10,10)$
O4V406040	0.182	N VB	0.29 ± 0.03	N	-409 ± 4 , (-480,-340) $\pm(10,10)$
O4V406040	0.182	C IVB	0.150 ± 0.004	N	-410 ± 1 , (-440,-380) $\pm(10,10)$
O4V406040	0.182	C IVR	0.075 ± 0.01	N	-409 ± 2 , (-440,-380) $\pm(10,10)$
O4V406050	0.221	N VB	0.42 ± 0.02	N,P?	-447 ± 2 , (-550,-350) $\pm(10,10)$
O4V406050	0.221	C IVB	0.22 ± 0.01	N	-425 ± 3 , (-480,-380) $\pm(10,10)$
O4V406050	0.221	C IVR	0.08 ± 0.02	N	-426 ± 3 , (-450,-390) $\pm(10,10)$
O4V407010	0.618	N VB	0.22 ± 0.03	P	(-590,-290) $\pm(20,10)$
O4V407010	0.618	Si IVB	0.17 ± 0.03	P	(-560,-170) $\pm(30,10)$
O4V407010	0.618	C IVB	0.38 ± 0.02	P	(-480,-260) $\pm(10,10)$
O4V407020	0.655	N VB	0.31 ± 0.02	P	(-510,-290) $\pm(20,10)$
O4V407020	0.655	Si IVB	0.20 ± 0.04	P	(-500,-170) $\pm(20,10)$

Table 2—Continued

Root name	Phase ^a	Line ^b	W_λ	Type ^c	V range ^d
O4V407020	0.655	C IVB	0.45 ± 0.05	P	(-480,-260) $\pm(20,10)$
O4V407030	0.695	N VB	0.35 ± 0.06	P	(-470,-290) $\pm(40,10)$
O4V407030	0.695	C IVB	0.41 ± 0.02	P	(-460,-270) $\pm(30,10)$
O4V407040	0.735	N VB	0.36 ± 0.04	P	(-530,-300) $\pm(20,10)$
O4V407040	0.735	C IVB	0.37 ± 0.02	P	(-440,-290) $\pm(10,10)$
O4V407050	0.774	C IVB	0.37 ± 0.02	P	(-400,-290) $\pm(10,10)$
<hr/>					
O4V408010	0.210	N VB	0.33 ± 0.01	N	$-399 \pm 1(-460,-340)\pm(10,10)$
O4V408020	0.247	N VB	0.33 ± 0.21	P	(-490,-220) $\pm(170,170)$
O4V408020	0.247	N VR	0.09 ± 0.01	N	$-397 \pm 2(-420,-350)\pm(10,10)$
O4V408020	0.247	Si IVB	0.42 ± 0.09	P	(-390,-150) $\pm(70,10)$
O4V408020	0.247	C IVB	0.24 ± 0.01	P	(-280,-170) $\pm(10,10)$
O4V408030	0.288	N VB	0.48 ± 0.06	P	(-550,-150) $\pm(10,10)$
O4V408030	0.288	N VR	0.20 ± 0.03	N	$392 \pm 1,(-450,-330)\pm(10,10)$
O4V408030	0.288	Si IVB	0.62 ± 0.02	P	(-470,-120) $\pm(10,10)$
O4V408030	0.288	C IVB	0.61 ± 0.03	P	(-490,-150) $\pm(10,10)$
O4V408040	0.327	N VB	0.53 ± 0.02	P	(-500,-160) $\pm(20,10)$
O4V408040	0.327	N VB	0.20 ± 0.03	N	$-402 \pm 4,(-460,-360)\pm(20,10)$
O4V408040	0.327	N VR	0.09 ± 0.03	N	$-404 \pm 4,(-440,-360)\pm(20,20)$
O4V408040	0.327	Si IVB	0.33 ± 0.02	P	(-450,-130) $\pm(10,10)$

Table 2—Continued

Root name	Phase ^a	Line ^b	W_λ	Type ^c	V range ^d
O4V408040	0.327	C IVB	0.58 ± 0.03	P	(-460,-140) $\pm(20,10)$

^aThe orbital phase of the mid-exposure time, using the ephemeris of Deeter et al. (1991)

^bB indicates blue doublet component and R indicates red doublet component

^cP=P Cygni line absorption; P?=possible P Cygni absorption, N=narrow absorption line

^dFor P Cygni absorption, we give the the range of heliocentric Doppler velocities (in km s^{-1}), while for the narrow absorption lines, we also give the centroid velocity.

Fig. 1.—

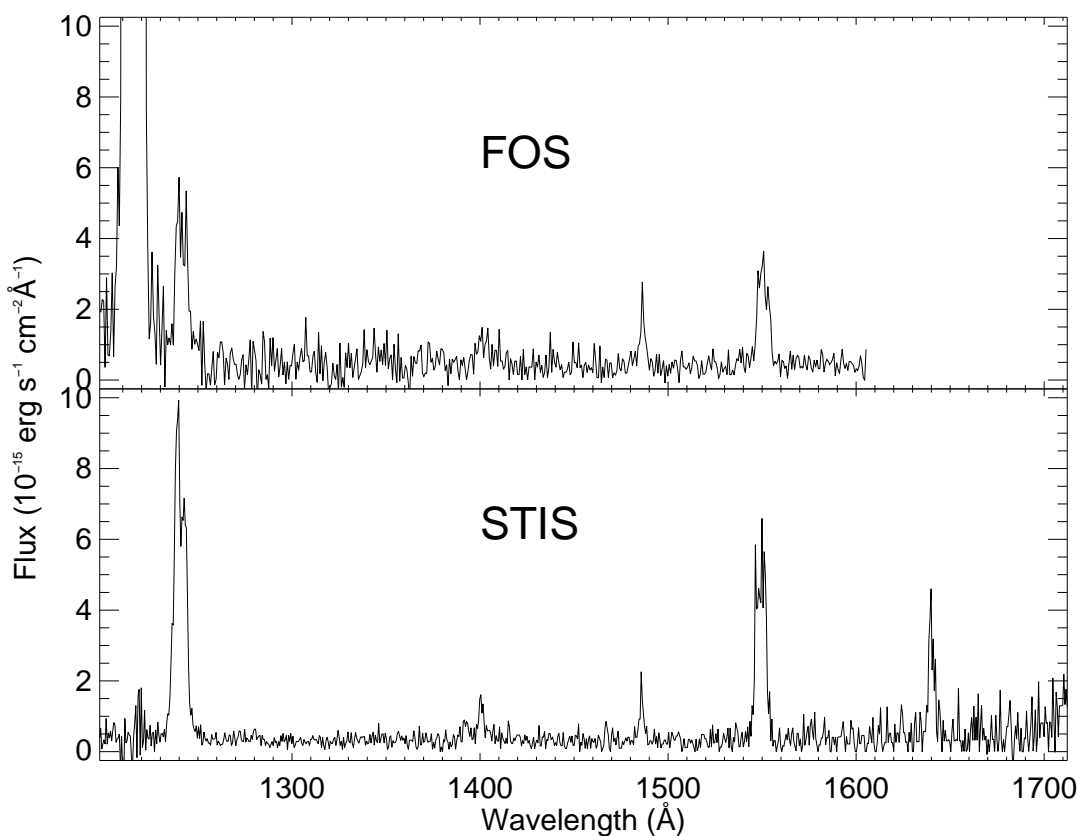


Fig. 2.—

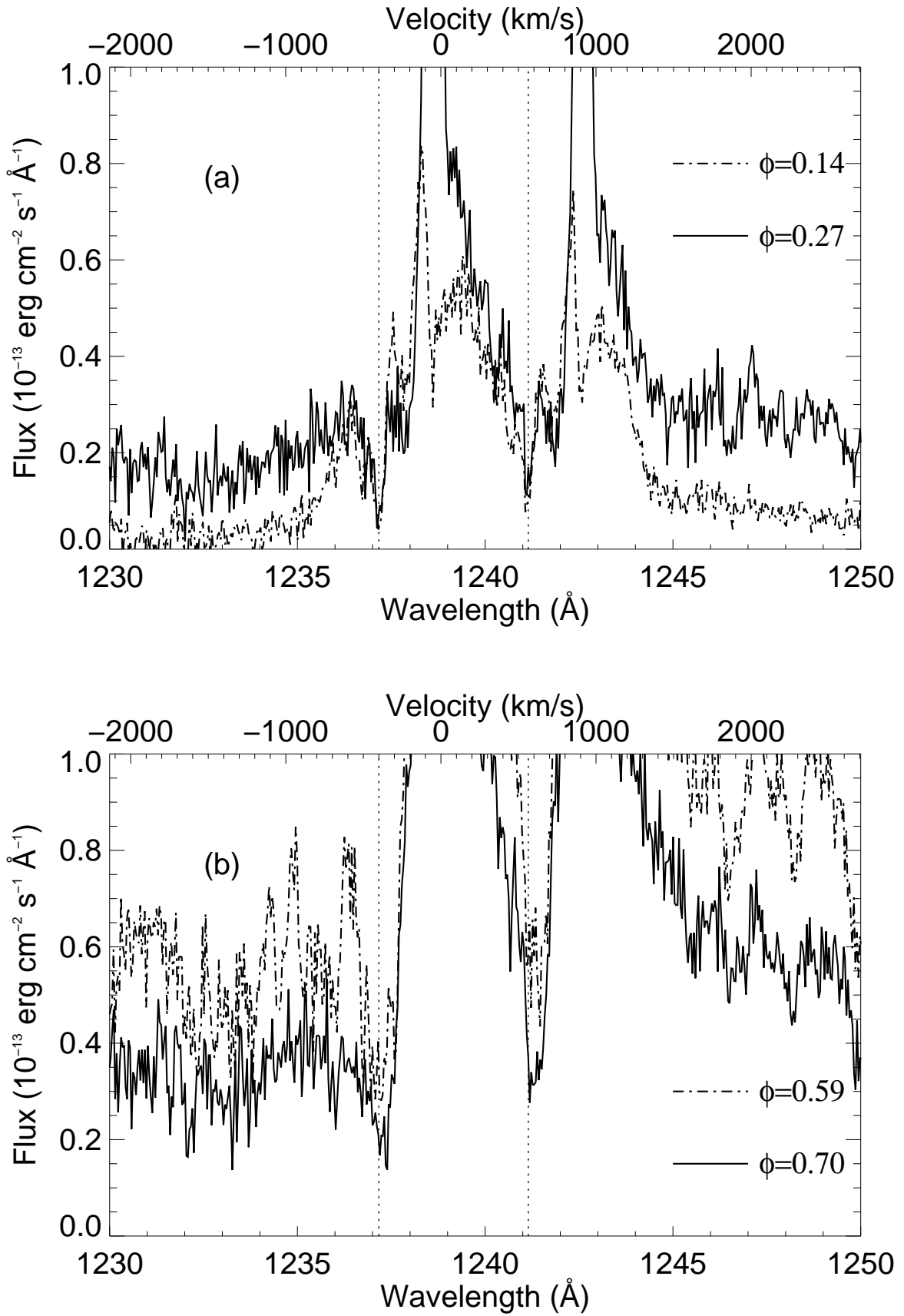


Fig. 3.—

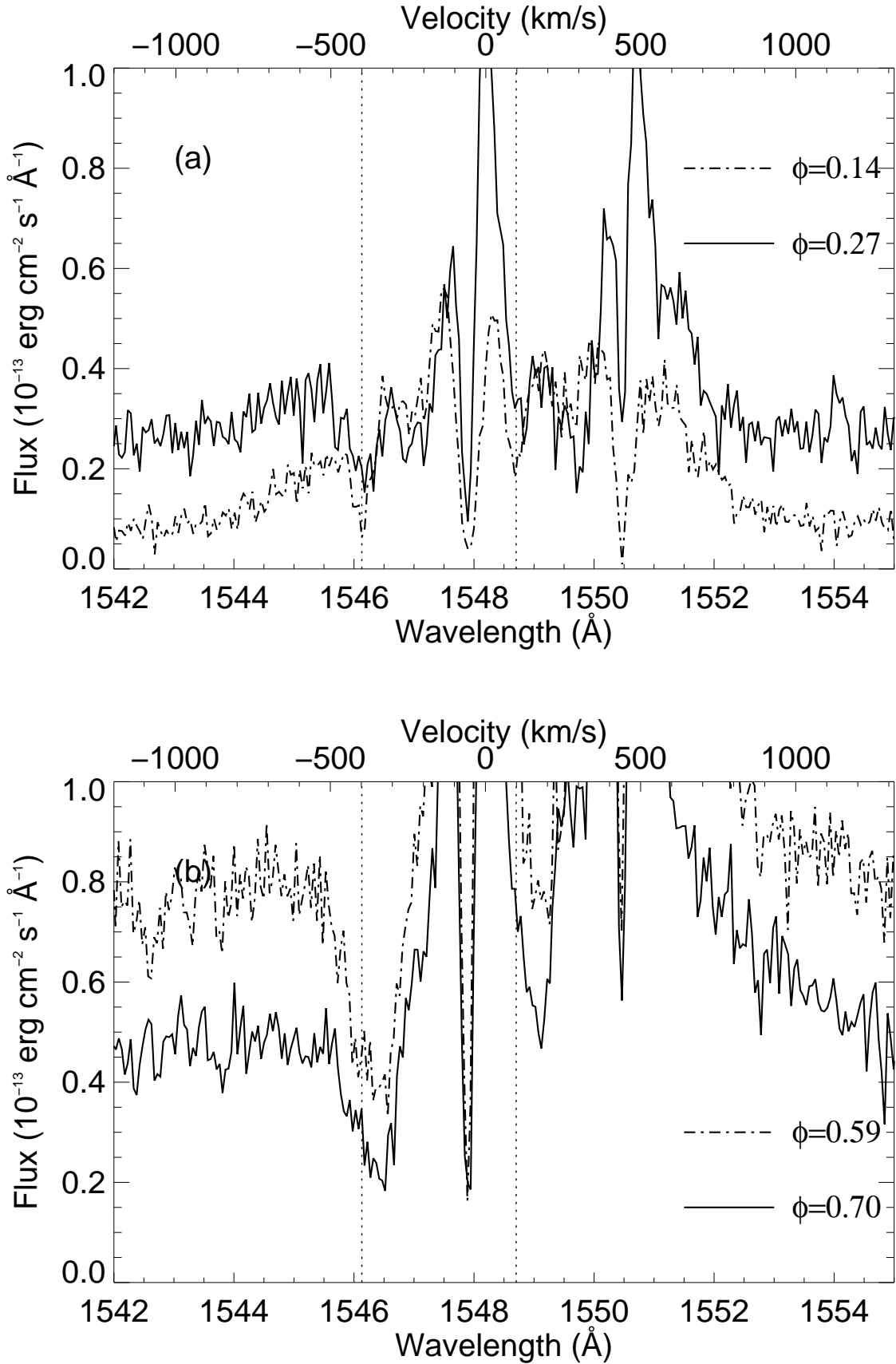


Fig. 4.—

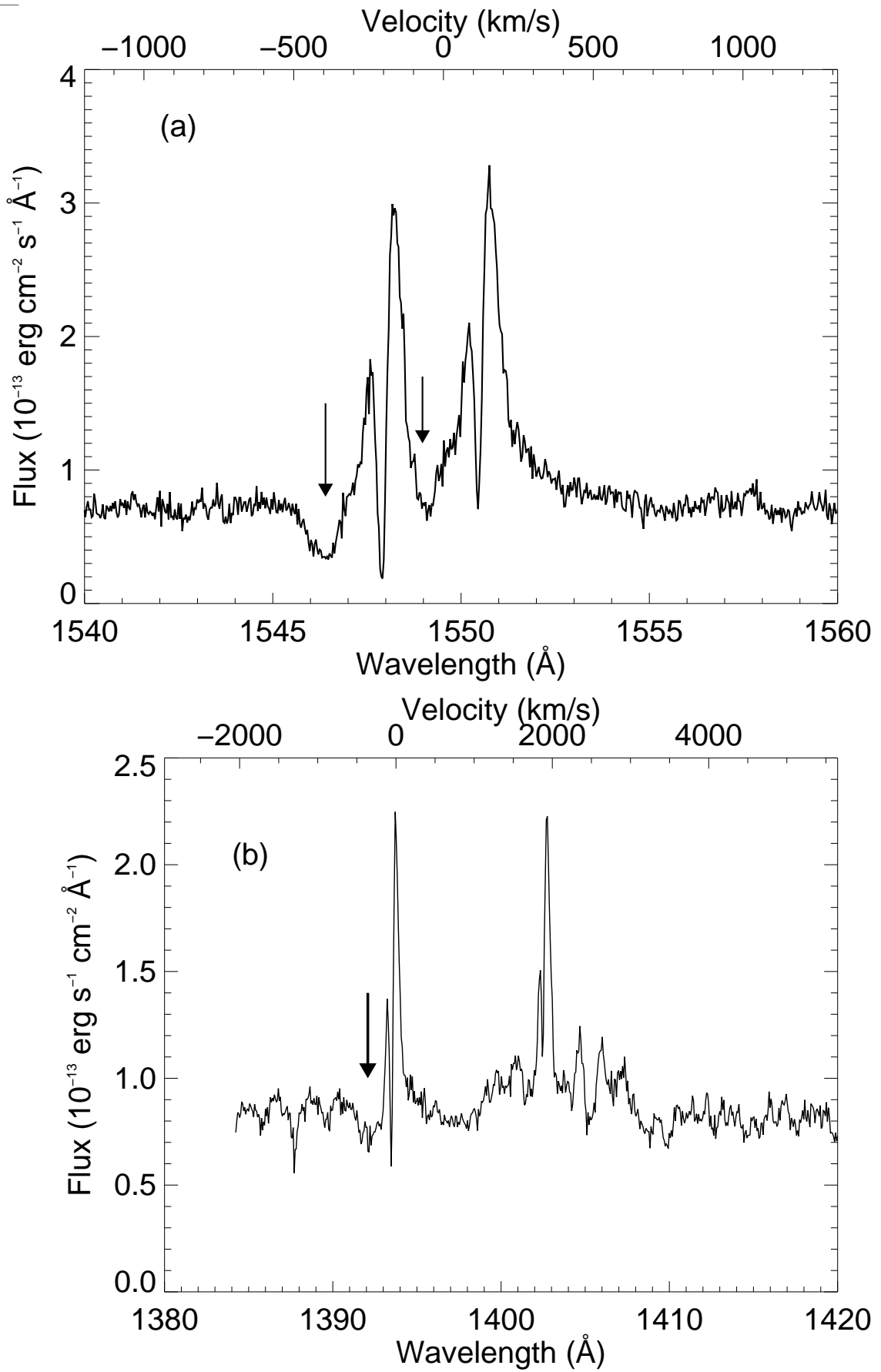


Fig. 4.—

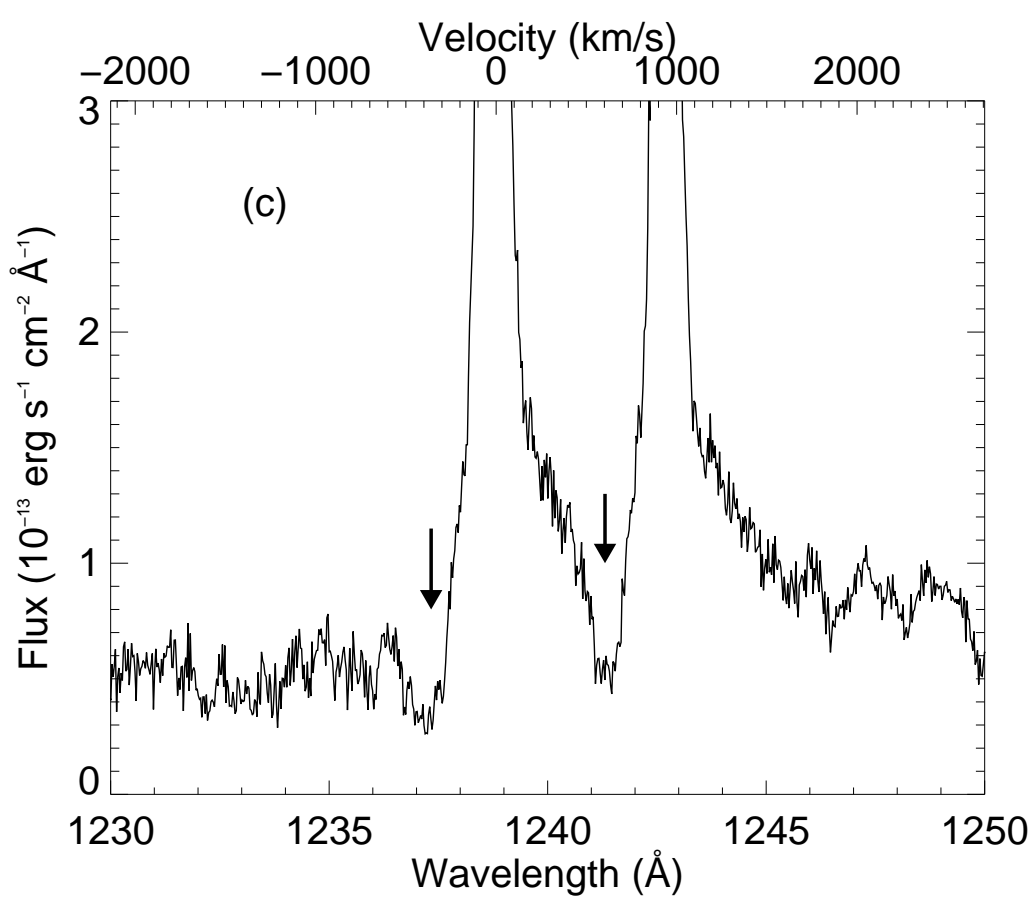


Fig. 5.—

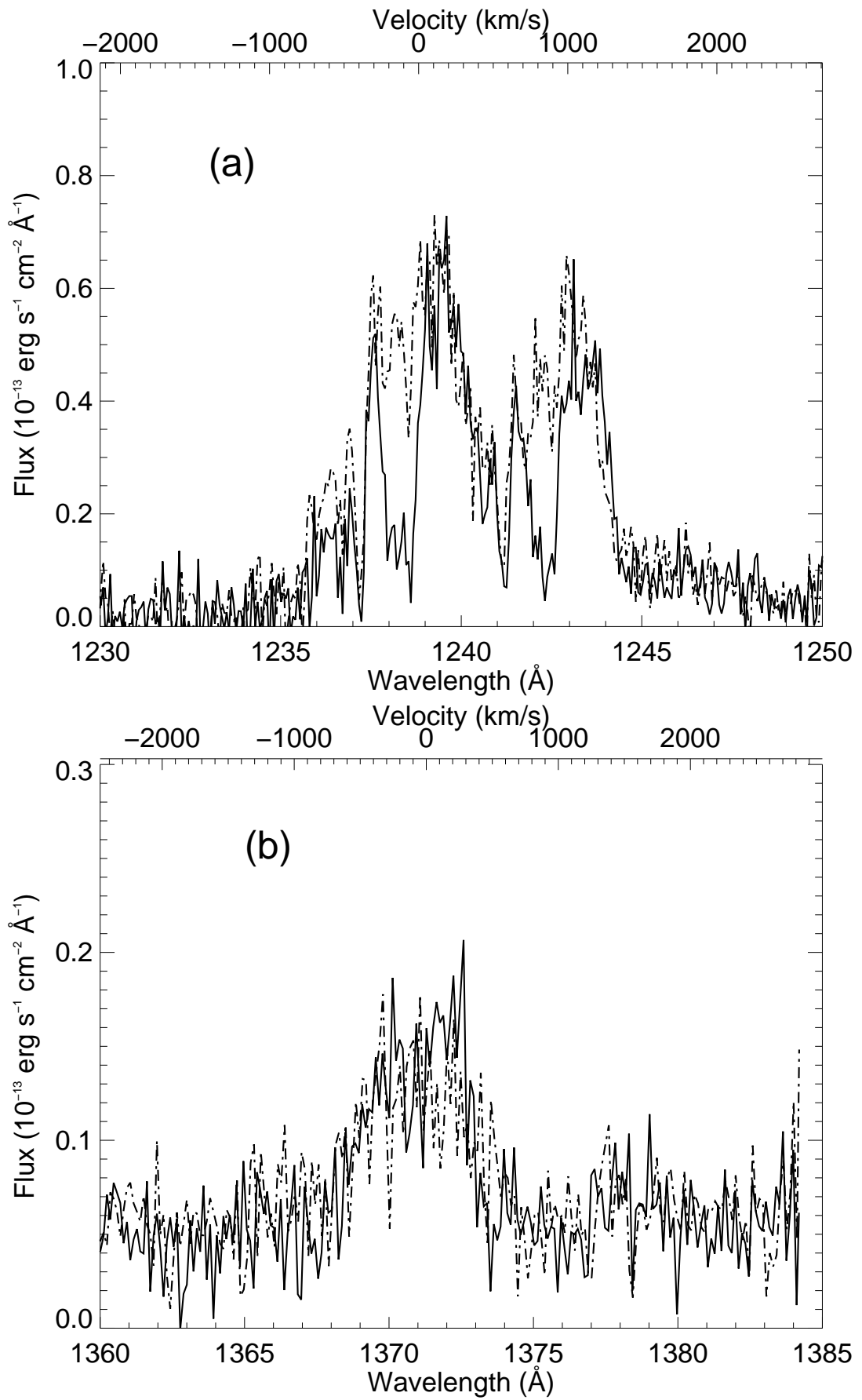


Fig. 5.—

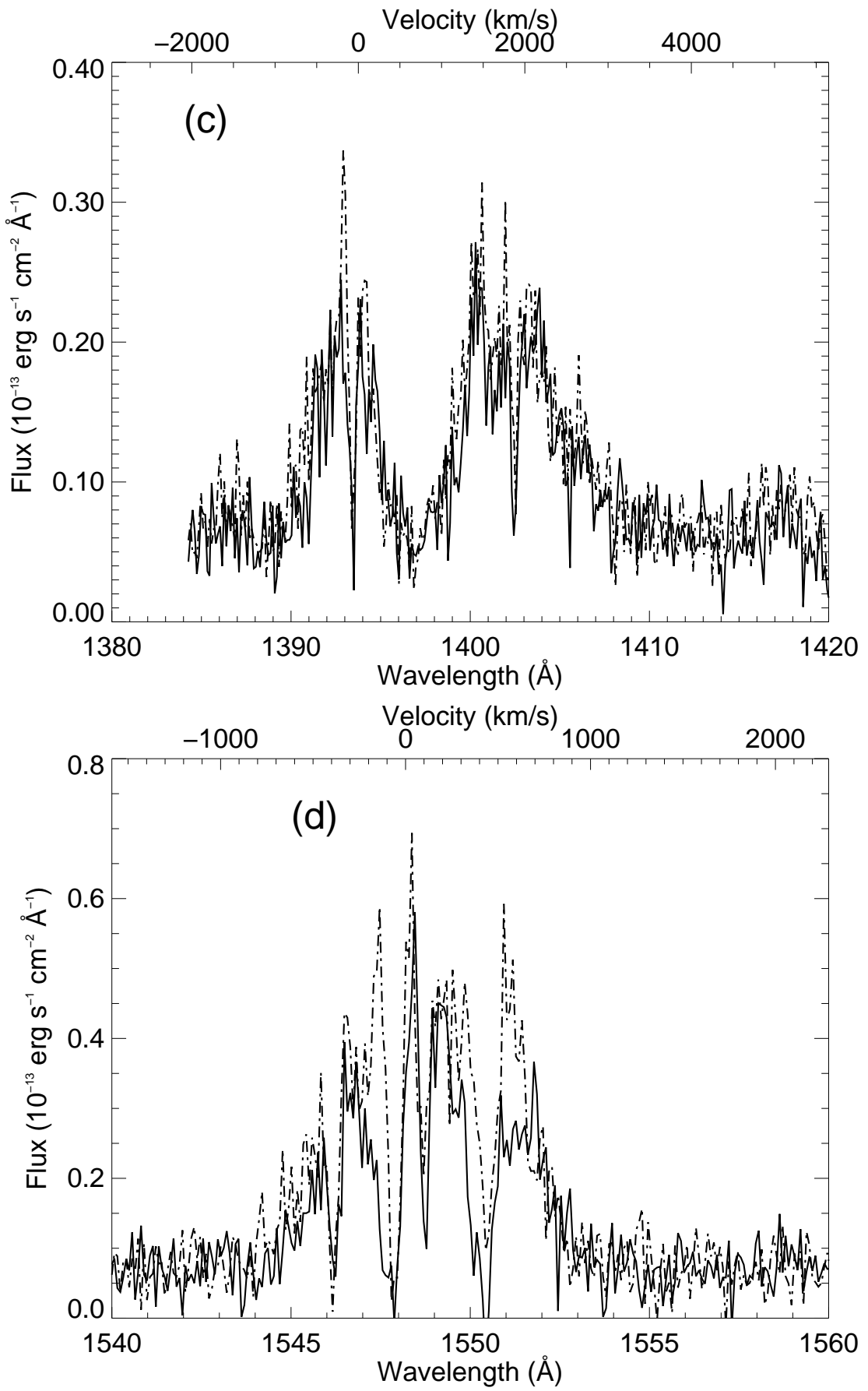


Fig. 5.—

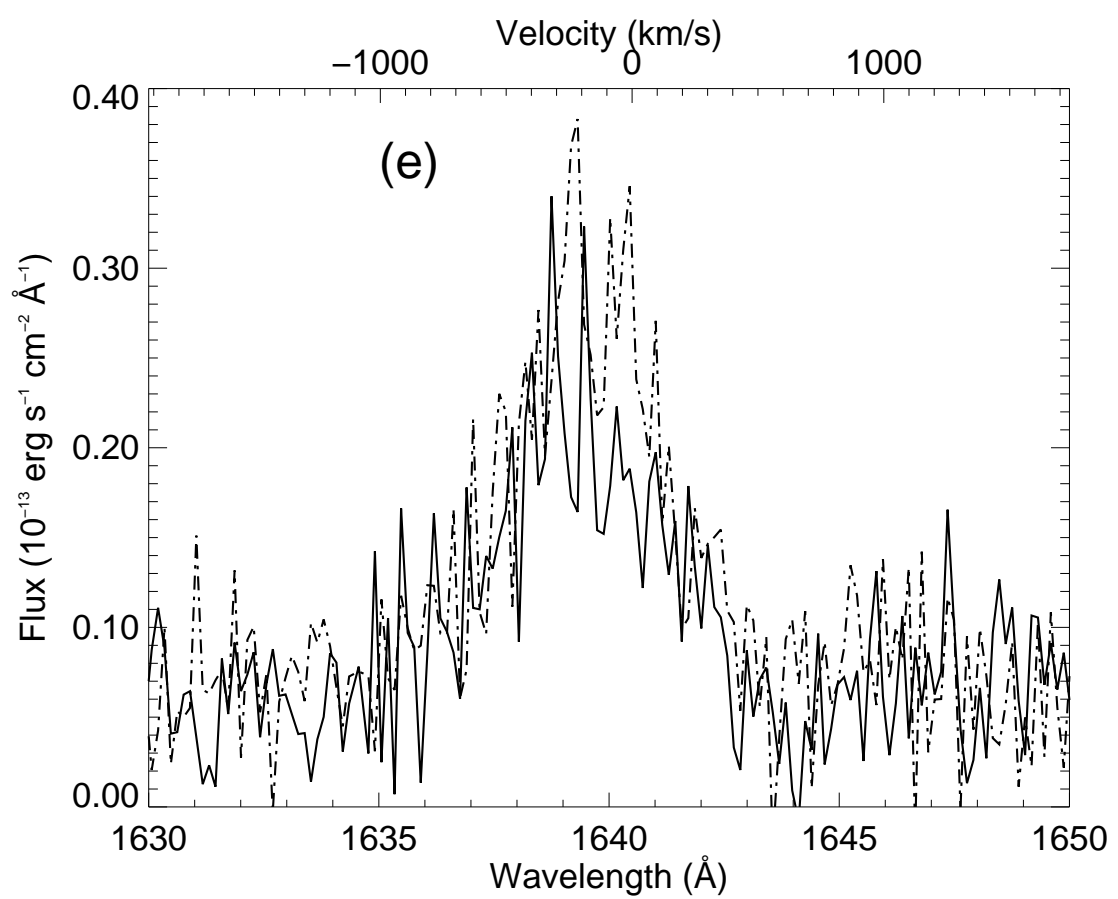


Fig. 6.—

